



Hybrid-heat effects on electrical-current aided friction stir welding of steel, and Al and Mg alloys



Jian Luo*, Wei Chen, Gen Fu

State Key Laboratory of Mechanical Transmission, College of Automotive Technology, Chongqing University, Chongqing 400030, PR China

ARTICLE INFO

Article history:

Received 14 April 2014

Received in revised form 3 July 2014

Accepted 4 July 2014

Available online 14 July 2014

Keywords:

Electric current aided friction stir welding

Hybrid heat effects

Microstructure

Microhardness

ABSTRACT

Electrical current aided friction stir welding (EFSW) is based on increasing heat generation during welding by adding a resistant heat source. The influence of current intensity to surface shaped features on welding seam was discussed. The comparison between AZ31B joints and Al 7075 joints was conducted. For the AZ31B joints, the resistant heat source promoted significant grain refinement and hardness improvement in the weld nugget zone (WNZ). It also increased plastic deformation during welding. For the Al 7075 joints, the grain size in the WNZ and heat affected zone (HAZ) increased slightly with the increase in electric current intensity. EFSW was proven to be suitable for joining high-strength alloys, such as 2Cr13Mn9Ni4 and Q235B. High microhardness values were obtained at both sides of the mechanical interlock zone.

© 2014 Elsevier B.V. All rights reserved.

1. Introduction

The application of friction stir welding (FSW) on the alloys of high-temperature melting points faces a serious tool wear problem (Çam, 2011). An effective solution to this problem is to add another heat source to the FSW process in order to increase heat generation during welding and hence improve thermoplasticization of the workpiece materials and reduce tool wear. Song et al. (2009) studied the microstructure and mechanical properties of a laser-FSW hybrid welding joint of Inconel 600, and found that hybrid FSW was 1.5 times faster than conventional FSW, and that the hybrid FSW joint had a 30% and 10% improvement in microhardness and tensile strength as compared to the joints formed with conventional FSW. Sun et al. (2013) studied laser-assisted FSW of carbon steel, and found that hybrid FSW enabled to expand the suitable welding technology ranges significantly and that the tool load and defects were decreased. Park (2009) used the finite element (FE) simulations to study the ultrasonic assisted FSW process and found that the ultrasonic vibration could reduce the welding force and obtain a joint with a better welding quality. Bang et al. (2013) employed preceding gas tungsten arc welding (GTAW) as a preheating heat source to join an Al6061-T6 aluminum alloy with a Ti-6%Al-4%V titanium alloy, and reported that elongation and joint strength of

the hybrid FSW welds increased significantly compared with those of the conventional FSW welds.

However, almost all of the hybrid friction stir welding methods mentioned above have a shortcoming—the hybrid heat sources are not simultaneously applied to the welding zone. The additional heat source is typically applied in front of the welding zone for pre-heating. It is difficult to combine the additional heat source with the friction heat source, which limits the applications of hybrid FSW. The present study introduces a new hybrid welding technology, which is the electrical current aided Friction Stir Welding (EFSW) process. Joints of two different light alloys, AZ31B Mg alloy and 7075 Al alloy, can be obtained through EFSW, and their microstructure and microhardness features under electric current variation are characterized and compared. In order to examine the feasibility of EFSW in welding high-strength alloys, EFSW was also conducted in 2Cr13Mn9Ni4 and Q235B dissimilar steels joint.

2. EFSW technique

As introduced by Luo (2007), EFSW is a hybrid welding technology, where electric current flows from the FSW tool, through the contact interface, into the workpieces, as shown in Fig. 1. Compared with the conventional FSW process, the EFSW technique utilizes resistant heat as an additional heat source. Hence more heat input should be generated during the EFSW process when keeping other parameters, such as welding speed and rotational speed, unchanged. A higher welding speed can be achieved under the same energy consumption. As reported by Luo et al. (2009),

* Corresponding author. Tel.: +86 23 65106195; fax: +86 23 65106195.

E-mail address: luojian2007@gmail.com (J. Luo).

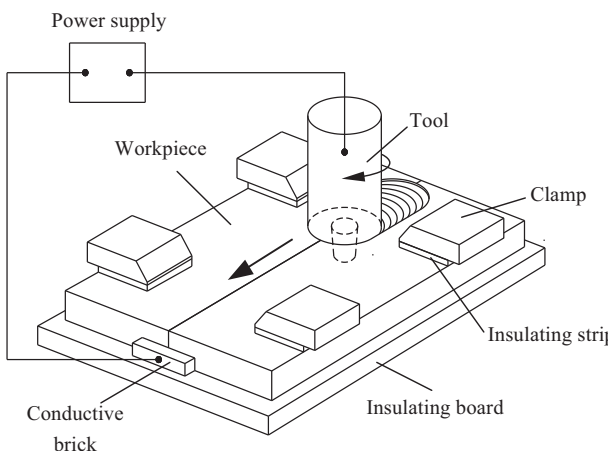


Fig. 1. Schematic diagram of electrical-current-aided friction stir welding.

the EFSW technique may improve welding efficiency, reduce welding defects, and extend the tool service life. Moreover, since EFSW allows a large heat generation, it extends the application range of the FSW technology by enabling welding of high-strength alloys.

The heat generation, Q_{EFSW} in the EFSW process includes two parts, Q_{FSW} , and Q_{res} , by FSW and electric resistance, respectively, shown in Eq. (1):

$$Q_{\text{EFSW}} = Q_{\text{FSW}} + Q_{\text{res}} \quad (1)$$

Q_{res} can be expressed as,

$$Q_{\text{res}} = I^2 R t$$

where I is the electric current density used in the EFSW process, t is the welding time, and R the effective resistance which contributes to the heat input in the EFSW process. During the lap welding process (Fig. 2), for example, the electric current should pass through two paths: (1) from the lower workpiece to the upper one, and then to the tool; and (2) from the lower workpiece directly to the tool through the pin. As shown in Fig. 2, the total resistance R involves seven components as shown in the expression

$$R = f(R_1, R_2, R_3, R_4, R_5, R_6, R_7) \quad (2)$$

where R_1 is the resistance of the welding shoulder, R_2 the contact resistance between the welding shoulder and the upper workpiece, R_3 the resistance of the upper workpiece, R_4 the contact resistance between the upper and the lower workpiece, R_5 the contact resistance between the pin and the upper workpiece, R_6 the contact resistance between the pin and the lower workpiece, and R_7 the resistance of the lower workpiece. Because the values of R_2 , R_4 , R_5 , and R_6 are much larger than those of R_1 , R_3 , and R_7 , it is apparently that the electrical contact resistances are the significant contributors of resistance heat Q_R generated during the EFSW process. Thus, Eq. (2) can be simplified as

$$R = f(R_2, R_4, R_5, R_6) \quad (3)$$

This consideration was also used in the resistance spot-welding analysis by Galler et al. (2010); the total resistance measured in this experiment fluctuates throughout the welding process, which might be a result of the electrical contact resistance fluctuation caused by temperature variation and the flow of the welded material. Babu et al. (2001) indicated that electrical contact resistance depended on the bulk resistivity, yield strength, and the number of contacting asperities. Song et al. (2005) found that contact resistance decreased when interface normal pressure was increased, although the effect of temperature on the weldment was complex. Rogeon et al. (2008) found that temperature and pressure were

Table 1
Chemical composition of 7075 Al alloy (in wt%).

Cu	Mn	Fe	Ti	Cr	Zn	Si	Mg	Al
1.4	0.3	0.5	0.2	0.18	6.1	0.4	2.2	Balance

two factors influencing the contact resistance during resistance spot welding. The fluctuation of the total resistance observed in the current study was consistent with what found in these researches.

3. Materials and experimental procedure

EFSW joints of 7075 aluminum alloy, AZ31B magnesium alloy, and dissimilar 2Cr13Mn9Ni4/Q235B steel were obtained in the present study. The chemical compositions of the four materials are shown in Tables 1–3.

The present study utilized several 5 mm thick plates of a AZ31B magnesium alloy and a hot rolled 7075 aluminum alloy to obtain EFSW butt joints. The rotating tool was made of a T12 carbon tool steel, which had a pin of 5 mm in diameter, 4.7 mm in length, and a shoulder with a diameter of 14 mm. A device with an input voltage of 220 V and an adjustable output current was used as the power supply for applying and controlling the electrical current. The anode of the power supply output was connected to the workpieces, while the cathode was connected to the spindle of the welding machine via an electrical brush. The workpieces were insulated from the work table by the mica sheets and the holding device so that a controllable electric current would flow from one side of the alloy plates to the tool during the welding process. The applied direct current density varied from 0 A to 150 A. In welding the plates of the AZ31B Mg alloy, a constant rotational speed of 1000 rpm and welding speed of 100 mm/min were used; while in welding the workpiece of the 7075 Al alloy, those were fixed at 940 rpm and 33 mm/min, respectively.

After the welding process, specimens were ground and polished. An ultrasonic cleaning machine was used to clean the samples. Then the AZ31B Mg alloy specimens were etched by a picric acid-acetic acid-alcohol solution (picric acid 3 g, acetic acid 20 ml, alcohol 50 ml, and distilled water 20 ml), and the 7075 Al alloy specimens were etched using 2% hydrofluoric acid. The transverse section of each obtained joint was investigated with an optical microscope to characterize the grain structure in different regions of each specimen. The microstructure of the samples was further evaluated using a scanning electron microscope (SEM).

The microhardness profiles across the middle portion of the joints were obtained on a microhardness tester with a load of 0.981 N and duration of 10 s. The interval between two successive dents was 1 mm.

In order to examine the feasibility of EFSW to weld high-strength alloys, 2 mm thick plates of 2Cr13Mn9Ni4 stainless steel and Q235B steel were also welded to obtain an EFSW lap joint. The 2Cr13Mn9Ni4 stainless steel was selected as the upper member of the lap welding. The rotating tool was made of tungsten carbide. It had a pin of 4 mm in diameter, 2 mm in length, and a shoulder of 20 mm in diameter. A tool rotational speed of 1000 rpm and welding speed of 50 mm/min were used, and the applied electrical current was about 1000 A. The tool tilt angle was set to 0° with respect to the vertical axis.

The 2Cr13Mn9Ni4 sides of the metallographic samples were etched by aqua regia, and the Q235 side by the nitric acid alcohol solution (volume ratio 4:96). The microstructure was then examined with an optical microscope and SEM. Vickers microhardness measurement was conducted with a load of 9.8 N and duration time of 10 s.

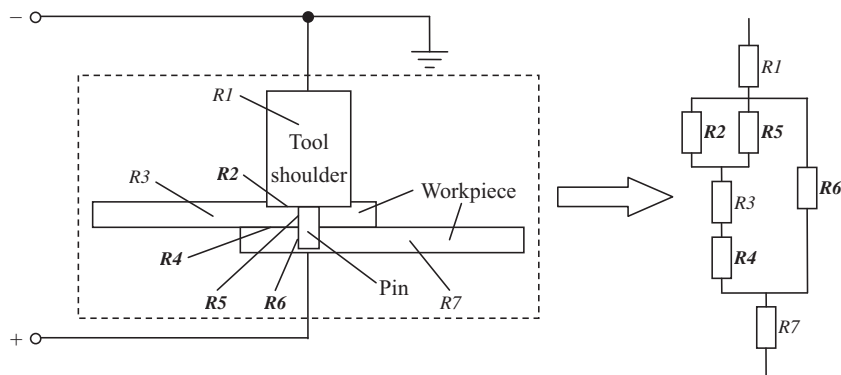


Fig. 2. Schematic of the resistances in the EFSW equipment.

Table 2

Chemical composition of AZ31B Mg alloy (in wt%).

Al	Zn	Mn	Ca	Si	Fe	Cu	Ni	Mg
2.5–3.5%	0.6–1.4%	0.2–1.0%	0.4%	≤0.1%	≤0.05%	≤0.05%	≤0.05%	Balance

Table 3

Chemical composition of 2Cr13Mn9Ni4 and Q235B steel (in wt%).

Steel	C	Mn	Ni	Cr	Si	S	P	Fe
2Cr13Mn9Ni4	0.15–0.2%	8.5–10.0%	3.7–5.0%	12.0–14.0%	≤0.8%	≤0.025%	≤0.035%	Balance
Q235B	0.12–0.20%	0.30–0.70%	–	–	≤0.30%	≤0.045%	≤0.045%	Balance

4. Results and discussion

4.1. EFSW of light alloys

4.1.1. Surface morphology

Fig. 3 shows the surface morphology of the aluminum welds under different electrical current. All the welds were obtained without surface defects except the one with the conventional FSW process (no electric current applied). A small segment of a shallow groove was detected on its advancing side, as illustrated in Fig. 3a. This groove defect was typically caused by insufficient heat input during the welding process. Because the resistance heat acted as an additional heat source during EFSW, the heat input was higher than that in the conventional FSW process under the same other parameters. As expected, the groove defect was avoided on EFSW joints (Fig. 3b–d).

Moreover, smoother weld surfaces were obtained with finer arc-shaped features as the applied electrical current was increased. As illustrated in the lower left of Fig. 4, the arc-shaped features were repeated marks appearing on the entire surface of the weld. Such a surface refinement effect of EFSW on the magnesium alloy was also reported previously by Luo et al. (2013). According to Wang and Feng (2003), a large amount of heat was generated between the tool shoulder and the workpieces during the welding process, forming a softened layer on the material surface. However, this model failed to consider the dynamic characteristic of material during welding process. If one separates a slice of the softened material as shown in Fig. 4, it is obvious that this slice was subjected to a shear force and friction force along the *y* axis, and a tensile force and friction force along the *x* axis. Under these forces the softened material would rotate and move forward with the shoulder. As more softened material was accumulated behind the shoulder, the friction force should increase until it exceeded the maximum shear or tensile force. Consequently, the back portion of the softened material would slough off. With the rotation of the tool, the detached material would finally form an arc-shaped mark. As the tool moved

forward, arcs were generated repeatedly and the arc-shaped features were eventually formed. Therefore, the distance between two adjacent arc-shaped marks depends on how far the softened material could advance with the shoulder before it sloughed off. In the present study, higher electrical current intensity resulted in finer arc-shaped features, i.e. a smaller distance between two adjacent arcs. This is because more heat generated under higher electric current, leading to a higher temperature in the weld. Since the shear and tensile forces are basically due to intermolecular interactions, an increase in the local temperature would cause the maximum values of both forces to decrease. As a result, the friction force exceeded the maximum shear or tensile force in a shorter period, which caused the back part of the softened material to be more quickly detached from the shoulder. Thus a smaller distance between two adjacent arcs, i.e. a smoother weld surface was formed (Fig. 3d).

4.1.2. Microstructure

Fig. 5 shows the microstructure of the base metal (BM) of the AZ31B magnesium alloy and the 7075 aluminum alloy. It can be observed that both BM of AZ31B have an equiaxed grain structure while the grains in the BM of 7075 Al alloy were elongated as a result of the rolling process.

Fig. 6 shows the optical microstructure of the AZ31B magnesium alloy joints. For the AZ31B magnesium alloy joints under electrical current, the grain size in the weld nugget zone (WNZ) was notably smaller than that of the conventional FSW joint. Within a certain range, the increase of current intensity would lead to the decrease of WNZ grain size. Fig. 7 shows the SEM image of the WNZ in AZ31B joints, from which one can see that the grains were significantly refined during welding under the electric current of 150 A. The minimum grain size was less than 1 μm (Fig. 7b), which is considered to be the size of ultra-fine grains. However, in the conventional FSW joint, the sizes of relatively small grains were about 8–10 μm approximately (Fig. 7a). The improvement can be attributed to the hybrid heat source in EFSW process, which caused the WNZ material to experience more remarkable plastic deformation under the

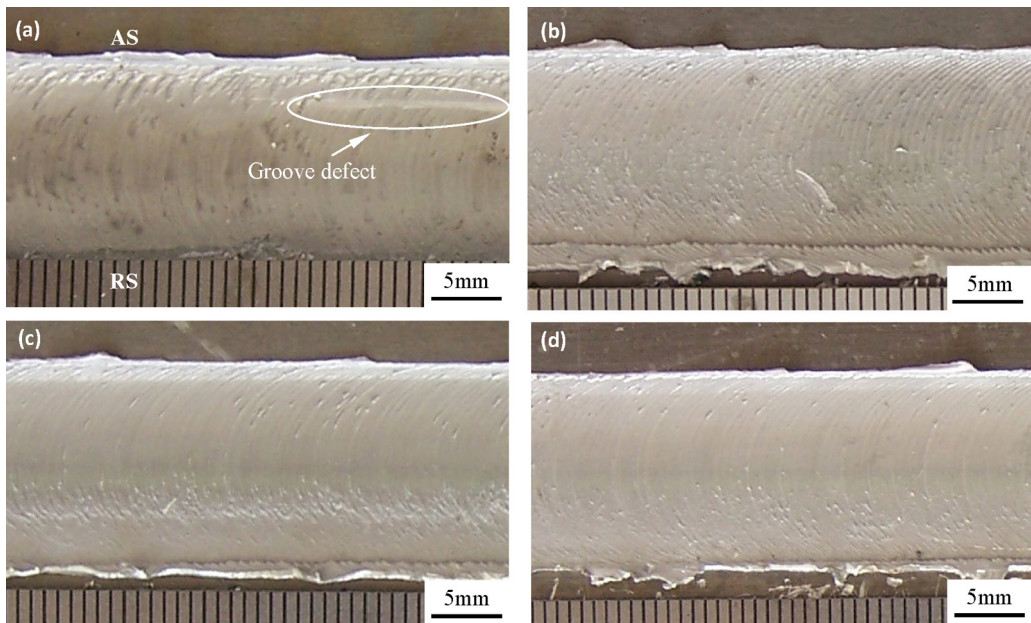


Fig. 3. Surface morphology of the aluminum welds obtained under electrical current of: (a) 0 A, (b) 50 A, (c) 100 A, and (d) 150 A. (AS: advancing side; RS: retreating side).

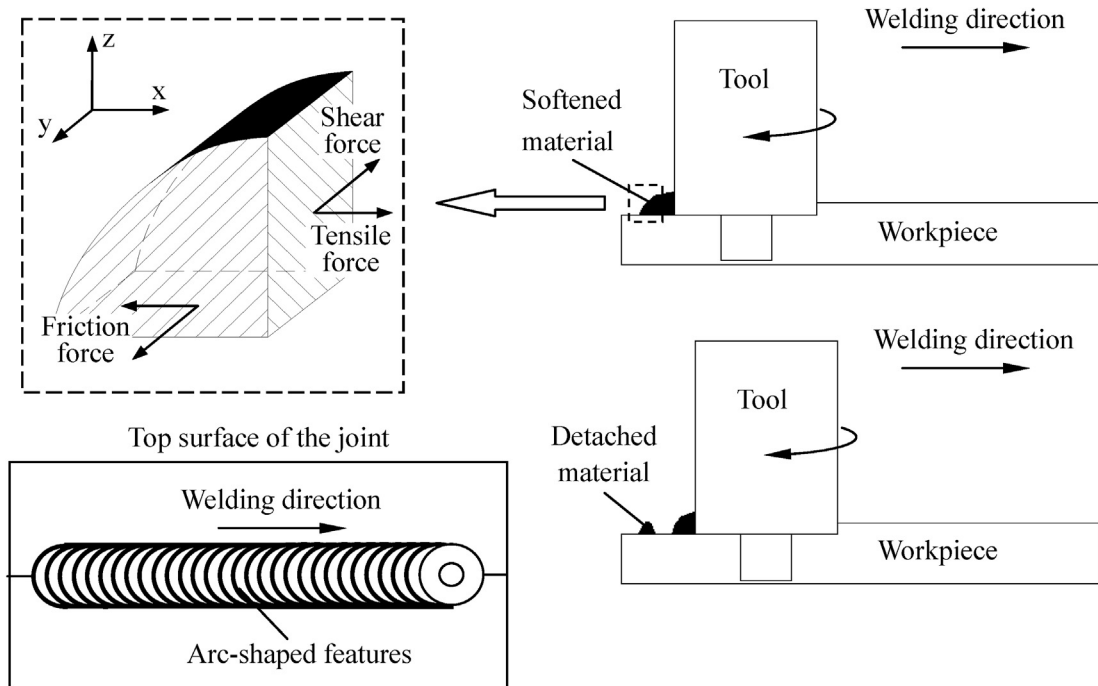


Fig. 4. Schematic of the arc-shaped features formation.

stirring effect of the pin; thus the grain fragmentation in the WNZ became more intensive. The nucleation rate of dynamic recrystallization was much higher in EFSW joints. These factors led to the smaller WNZ grain size under a larger electric current.

Grains in the thermo-mechanically affected zone (TMAZ) exhibits no characteristic of elongation, which is consistent with other experimental results on the TMAZ microstructure of the FSW magnesium alloy joints, such as the AZ31 joints obtained by Khodir and Shibayanagi (2007) and the AZ31B joints by Afrin et al. (2008). Grain size in the TMAZ of EFSW joints was similar to that of the conventional FSW joint. However, it can be seen that the TMAZ grains of EFSW joints were more uniform than that in the conventional FSW joint. The reason is that the EFSW joint experienced a higher

peak temperature under the effect of the hybrid heat source than did the conventional FSW joint, so that dynamic recrystallization took place more rapidly and more thoroughly, which led to more uniform grain structure in the TMAZ of EFSW joints. Fig. 8 shows the SEM image of the TMAZ in AZ31B joints. Twin crystals can be found in the EFSW joint under electrical current of 150 A (Fig. 8b), while no such a structure can be detected in the conventional FSW joint (Fig. 8a) where, limited plastic deformation occurred in TMAZ due to the low energy input in the welding process. However, during the EFSW welding process, the energy input at the TMAZ is large enough to allow the plastic deformation of twinning to take place because of the resistant and frictional heat.

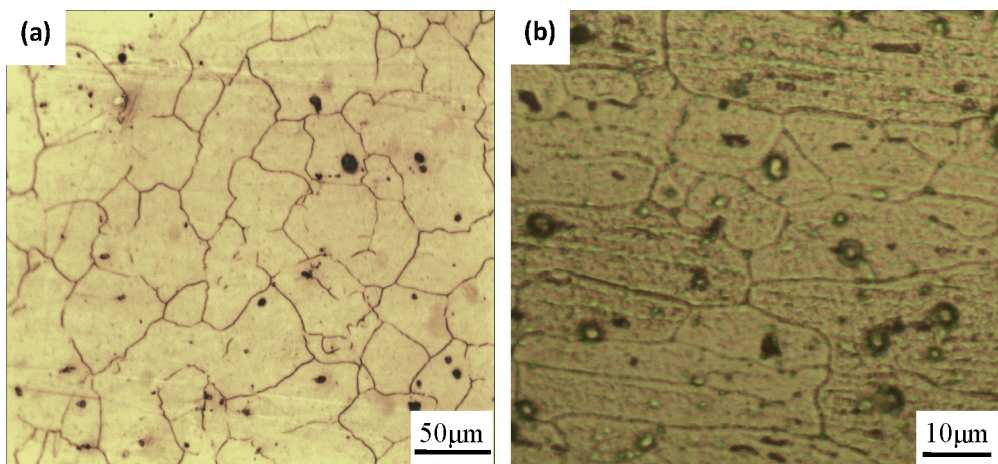


Fig. 5. Optical microstructure of transverse sections of the base metal of: (a) AZ31B magnesium alloy and (b) 7075 aluminum alloy.

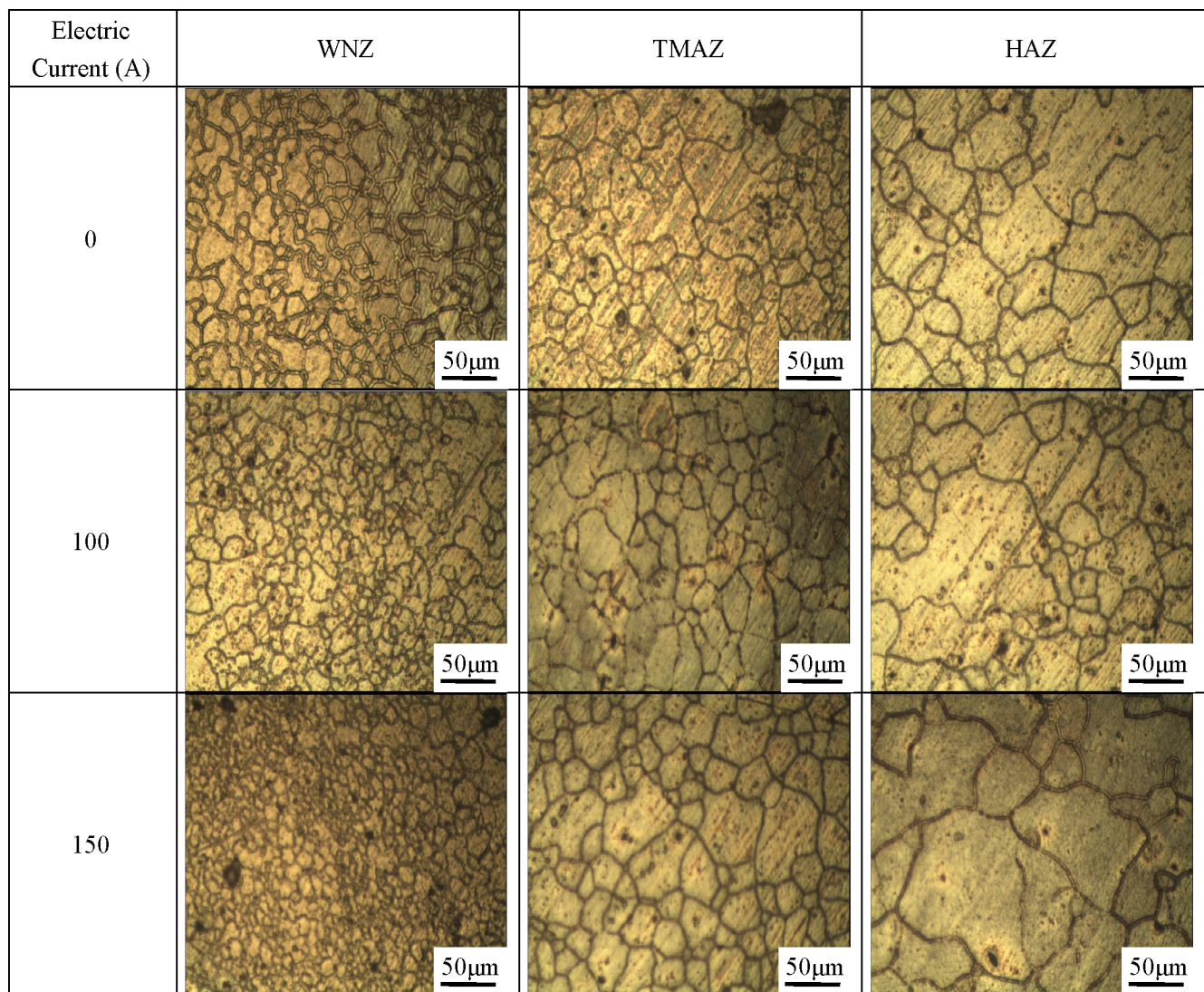


Fig. 6. Optical microstructure of transverse sections of AZ31B magnesium alloy joints.

In the heat affected zone (HAZ), the grain size of the conventional FSW was the finest; while the EFSW joint under current of 150 A had the coarsest grains, which was approximately 150 μm . This phenomenon may be attributed to the longer period of high

temperature exposure in the HAZ of the EFSW joints than that of the conventional FSW joint. Therefore, one may reason that for AZ31B EFSW joints, the HAZ is also a weak zone, but the WNZ has a better performance compared with the conventional FSW joints.

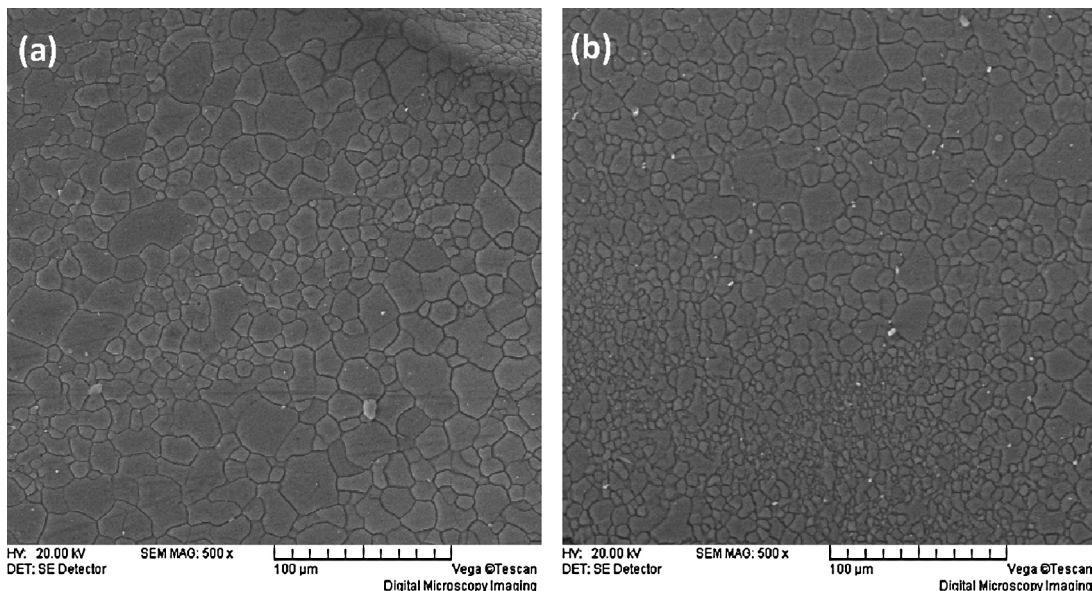


Fig. 7. WNZ microstructure of transverse sections of the AZ31B joints under electric current of: (a) 0 A and (b) 150 A.

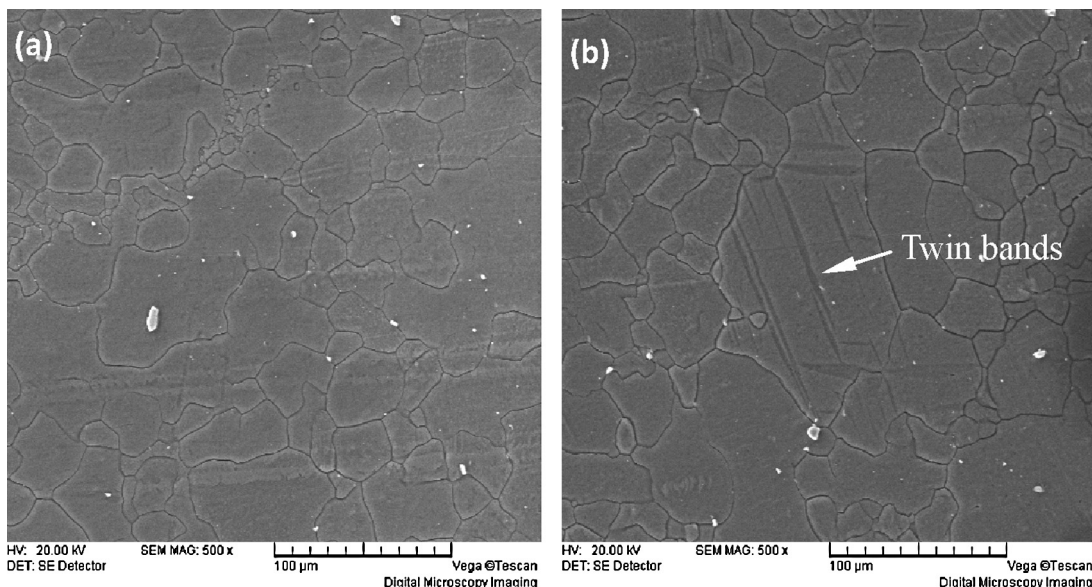


Fig. 8. TMAZ microstructure of transverse sections of the AZ31B joints under electric current of: (a) 0 A and (b) 150 A.

It is known that typically the WNZ and the TMAZ are critical zones in the FSW joints. As reported by Yang et al. (2010), the failure location of the AZ31 joints shifted from the TMAZ to the WNZ due to the increase of the tool shoulder diameter. Ilman and Kusmono Iswanto, 2013 reported that all the welded AA2024-T3 specimens exhibited fracture in the WNZ. Because of the softening phenomenon during recrystallization, the WNZ usually becomes a weak zone, especially in the FSW joints of light alloys, as documented in previous researches (e.g., Santos et al., 2011). However, in EFSW of the AZ31B Mg alloy, the WNZ microstructure was significantly refined by the hybrid heat effect; the TMAZ had more uniform grains and twin crystals; while the HAZ grains were coarsened due to the relatively high heat input. Therefore, one can anticipate that the weakest zone of EFSW joints was the HAZ rather than the WNZ or TMAZ.

Fig. 9 shows the optical microstructure of the 7075 aluminum alloy joints, which did not exhibit a variation pattern similar to that in the AZ31B joints as a result of electrical current change. The

current variation from 0 to 150 A made the average WNZ grain size in Al the 7075 joints slightly increase from 7 μm to 11 μm approximately, which might be due to the longer grain growth time caused by a higher heat input. This suggested that the WNZ of AZ31B and Al 7075 joints responded differently to the variation of heat input and plastic deformation, which might lead to a difference in the nucleation rate of recrystallization and the extent of grain growth under similar conditions. The TMAZ has a highly directional grain zone, which is a mixture of equiaxed grains and elongated grains. The elongated grains were obtained from deformation during welding while the equiaxed grains might have originated from dynamic recrystallization. The additional electric current made the strip-shaped grains less narrow and more equiaxed, which might be attributed to recovery of grain. A slight increase in grain size with the increase in electrical current intensity was also detected in the HAZ.

The SEM images of microstructure in the Al 7075 EFSW joints are shown in Fig. 10, from which one can see that the

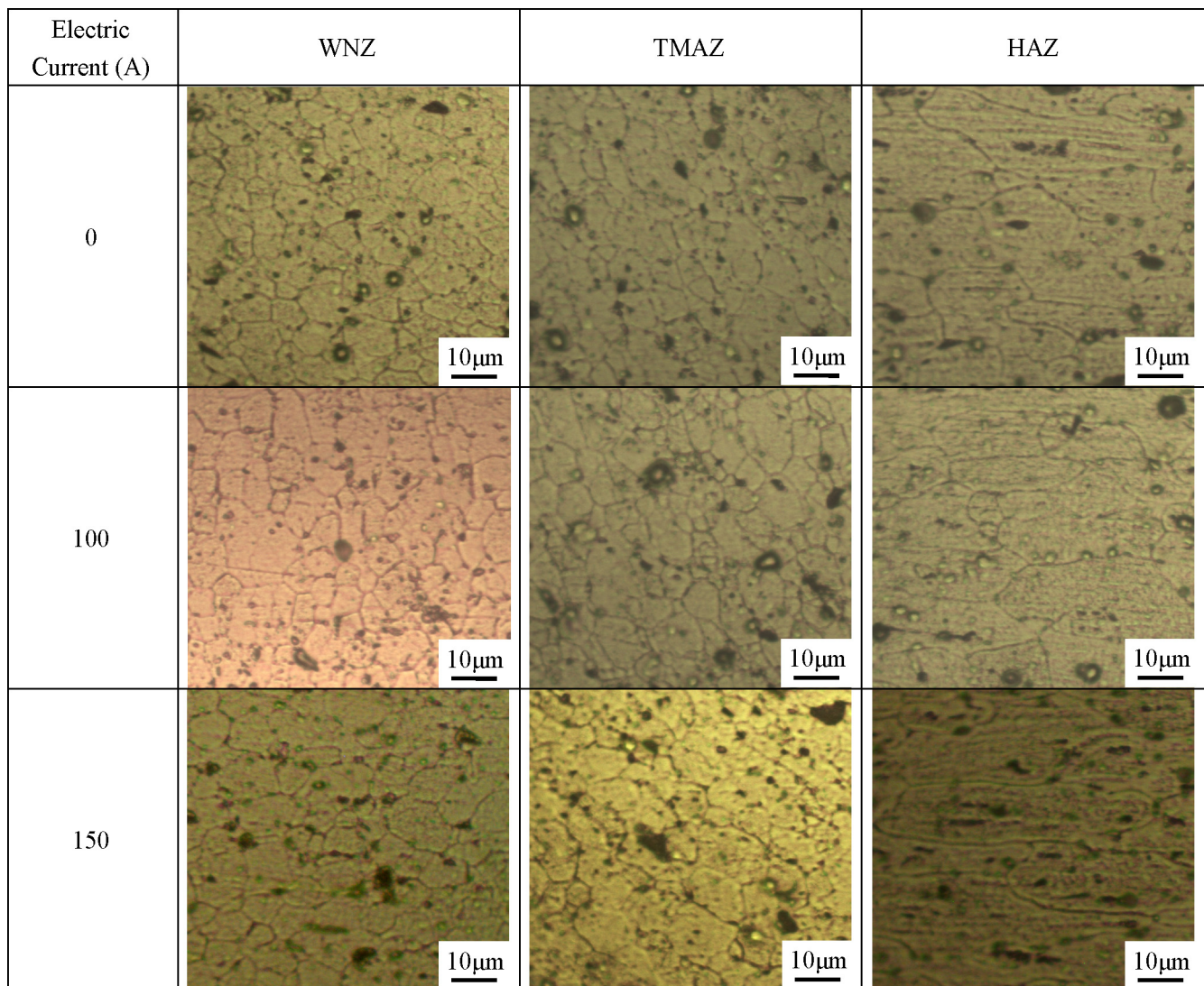


Fig. 9. Optical microstructure of transverse sections of 7075 aluminum alloy joints.

second-phase particles are distributed among the matrix grains. Since the second-phase particles are less vulnerable to corrosion than the matrix material, the etching process removed the material around some of these particles, detaching them from the

matrix. As a result, a number of small pits were formed after etching, as shown in Fig. 10a. The WNZ contained fine and dispersed second-phase particles (Fig. 10a). In the TMAZ, some particles were elongated showing a directional character similar to the TMAZ grain

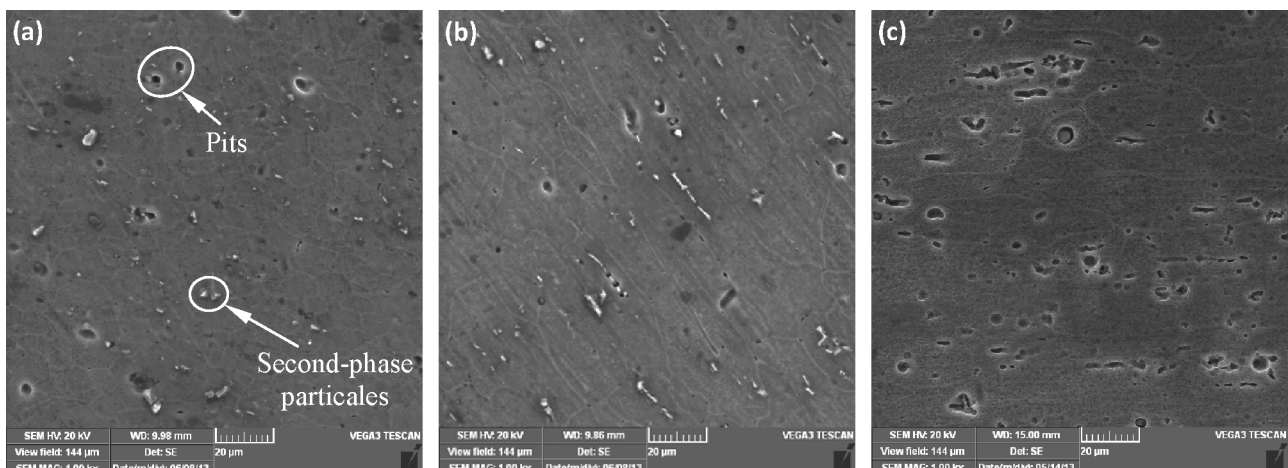


Fig. 10. SEM micrographs of transverse sections in the EFSW joint of the 7075 Al alloy: (a) WNZ, (b) TMAZ, and (c) HAZ.

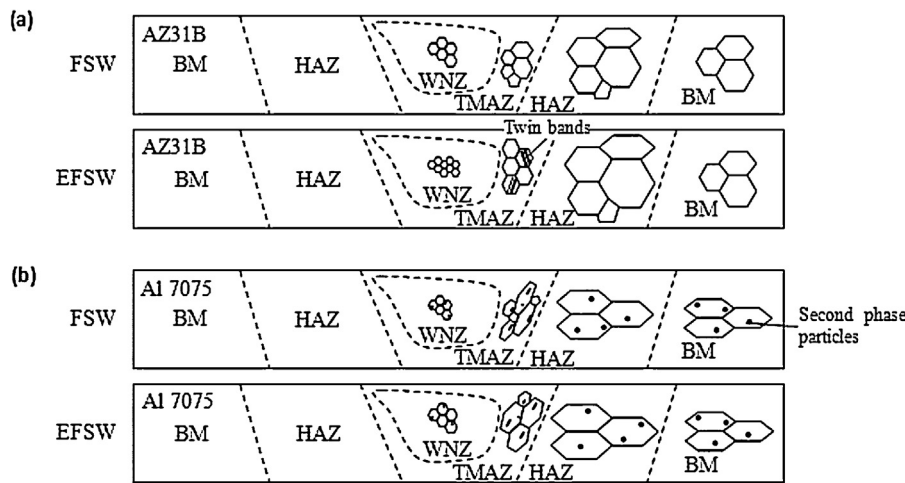


Fig. 11. Schematic of hybrid heat effects on the microstructural characteristic of: (a) AZ31B joints and (b) Al 7075 joints.

structure (Fig. 10b). The HAZ had coarser second-phase particles than the WNZ (Fig. 10c). As stated by Chang et al. (2009), when second-phase particles exist in the alloys, grain growth is impeded due to the obstacle effect of dispersed particles on grain boundary migration. This may explain why the microstructure of the WNZ, TMAZ, and HAZ only exhibited a limited extent of grain growth in the field of electrical current.

Fig. 11 illustrates the hybrid heat effects on the microstructural characteristic of AZ31B and Al 7075 joints. For AZ31B joints, the hybrid heat effects remarkably refined WNZ grains and brought more uniform microstructure, as well as twin crystals in the TMAZ; while in HAZ the hybrid heat resulted in a large grain size due to a high heat input. For the Al 7075 joints, the hybrid heat slightly coarsened the grains in the WNZ and HAZ, causing the elongated grains in the TMAZ to become more equiaxed probably in recovery.

4.1.3. Microhardness

Fig. 12 shows the microhardness distributions of the AZ31B and Al 7075 joints. For the AZ31B Mg alloy, the WNZ microhardness of the EFSW joints is higher than that of the base metal (the average BM hardness is about 60 HV), while the WNZ microhardness of the conventional FSW joint was lower than that of the base metal (Fig. 12a). It was obvious that the maximum WNZ microhardness (around 85 HV) appears in the EFSW joint under 150 A electric current, and the minimum value (around 43 HV) appears in the conventional FSW joint. This characteristic can be attributed to the fine grain strengthening in the WNZ of EFSW

joints. In the conventional FSW joint, the low WNZ microhardness was due to the softening effect during the recrystallization process.

Increase in the electrical current, increases the TMAZ microhardness of the AZ31B joints. This is because of the twin strengthening mechanism in the TMAZ of EFSW joints. The TMAZ microhardness of the conventional FSW joint was almost the same as that of AZ31B base metal.

The conventional FSW AZ31B joint shows the highest HAZ microhardness, which is approximately 52 HV; while the EFSW joint under 150 A current exhibits the lowest HAZ microhardness. The relatively coarser grains in the HAZ of AZ31B EFSW joints should have resulted in a lower microhardness than that of the conventional FSW joint.

However, in the 7075 Al alloy joints, slight disparity in microhardness exists between different joints (Fig. 12b). This result may be attributed to the small microstructural difference under different electric current intensity. Contrary to the microhardness profile of AZ31B joints, the microhardness in the WNZ and TMAZ slightly decrease with the increase in electrical current because of the increase in the gain size. The minimum microhardness value (around 46 HV) can be found at the HAZ of the EFSW joint under 150 A current. Recrystallization in WNZ did not induce the significant softening effect as in the conventional FSW AZ31B joint, probably due to the fact that the fine and dispersed second-phase particles in the WNZ provide a strengthening mechanism and cause an increase in the microhardness in this area.

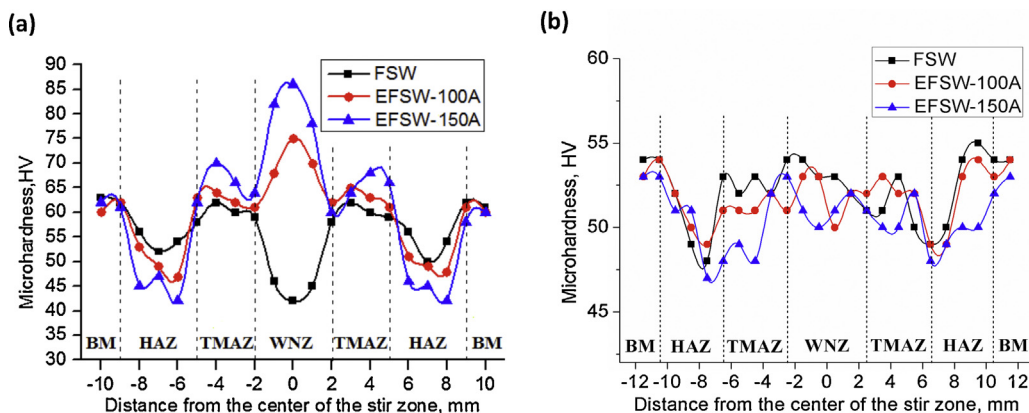


Fig. 12. Microhardness distributions of: (a) AZ31B Mg alloy joints and (b) 7075 Al alloy joints.

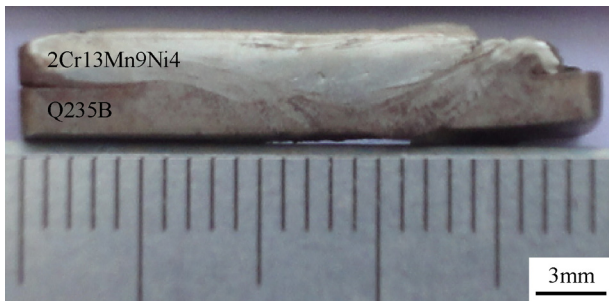


Fig. 13. The transverse section of the 2Cr13Mn9Ni4/Q235B joint by EFSW.

4.2. EFSW of steel

It is very difficult to apply the FSW on high-strength alloys because of the insufficient heat generation to plasticize the high molten point welded material during FSW. However, by combining a resistance heat source with the friction heat source, this problem may be alleviated or eliminated through EFSW. In the present study, the EFSW lap joint of 2Cr13Mn9Ni4 and Q235B was obtained successfully without damaging the stir pin. Fig. 13 shows the cross-section of the 2Cr13Mn9Ni4/Q235B steel dissimilar metal joint by EFSW. It can be observed that the 2Cr13Mn9Ni4/Q235B joint was achieved without any welding defects by the EFSW.

4.2.1. Microstructure

Fig. 14 is the microstructure of the 2Cr13Mn9Ni4/Q235B dissimilar lap joint by EFSW. There are three characteristic regions in the dissimilar joint: the 2Cr13Mn9Ni4 side, the Q235B side, and the mechanical interlock zone. The mechanical interlock zone can be easily observed in dissimilar joints obtained by conventional FSW, as reported by Fazel-Najafabadi et al. (2011). It was produced by the plastic flow of two dissimilar materials during the FSW process.

The microstructure of the 2Cr13Mn9Ni4 base metal consists of only the austenite phase, as shown in Fig. 14a. However, acicular martensite was formed at the 2Cr13Mn9Ni4 side adjacent to the mechanical interlock zone, as shown in Fig. 14b. The mechanical interlock zone appears in the connecting area between 2Cr13Mn9Ni4 and Q235B. Due to the effect of friction and resistance hybrid heat generation, the material in the WNZ was rapidly transformed into a thermoplastic state. Thus the thermoplastic materials flowed together at the interface of the dissimilar metal welding joints, and formed the mechanical interlock zone after the welding process. The microstructure in the mechanical interlock zone comprised austenite and pearlite. Furthermore, Fig. 14c and d reveals that more austenite structure appeared in the mechanical interlock zone near the 2Cr13Mn9Ni4 side, while more pearlite structure appears in the mechanical interlock zone near the Q235B side.

Fig. 14e shows an obvious interface between the Q235B side and the mechanical interlock zone, and some martensite structure was formed at the Q235B side near the interface. The microstructure of the Q235B base metal was composed of some pearlite and a low content of ferrite (Fig. 14f).

To further study the microstructure of the Q235B near the interface, only the microstructure at the Q235B side was etched and SEM images were obtained and shown in Fig. 15. A distinct interface exists between the mechanical interlock zone and the Q235B side, and no welding defects were found at the interface. Large grain size appears near the interface, and lath martensite was formed (Fig. 15a and b), while the Q235B base metal shows a fine grain structure (Fig. 15c). The formation of the large lath martensite can be attributed to the hybrid heat generation in the EFSW process. Martensite should be formed at both the 2Cr13Mn9Ni4 and the Q235B sides, as well as near the mechanical interlock zone. However the microstructure at the 2Cr13Mn9Ni4 side consisted of acicular martensite, while that at the Q235B side consisted of lath martensite. This is owing to the different carbon contents and cooling speeds in the two areas. Compared with the 2Cr13Mn9Ni4 side,

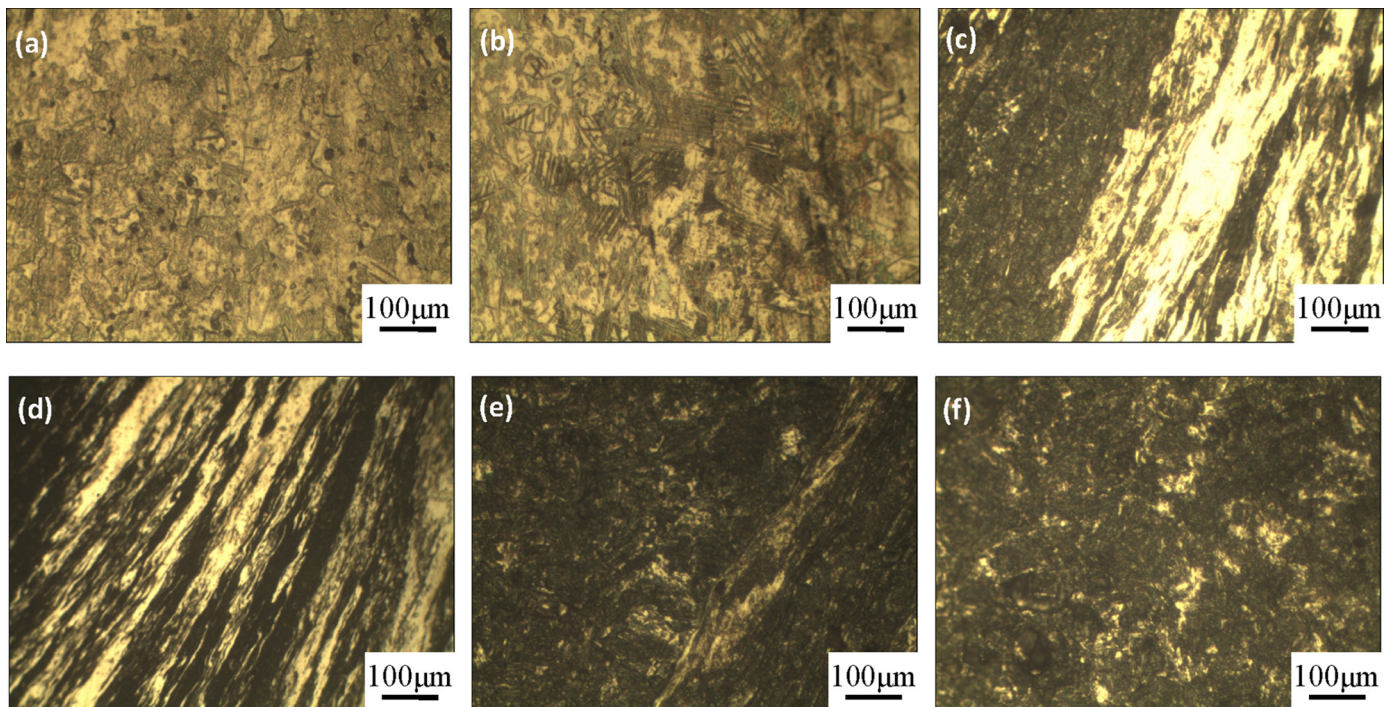


Fig. 14. Microstructure of transverse sections of the 2Cr13Mn9Ni4/Q235B joint in: (a) 2Cr13Mn9Ni4 base metal, (b) the 2Cr13Mn9Ni4 side adjacent to the mechanical interlock zone, (c) the mechanical interlock zone near the 2Cr13Mn9Ni4 side, (d) the mechanical interlock zone near the Q235B side, (e) the Q235B side adjacent to the mechanical interlock zone, and (f) Q235B base metal.

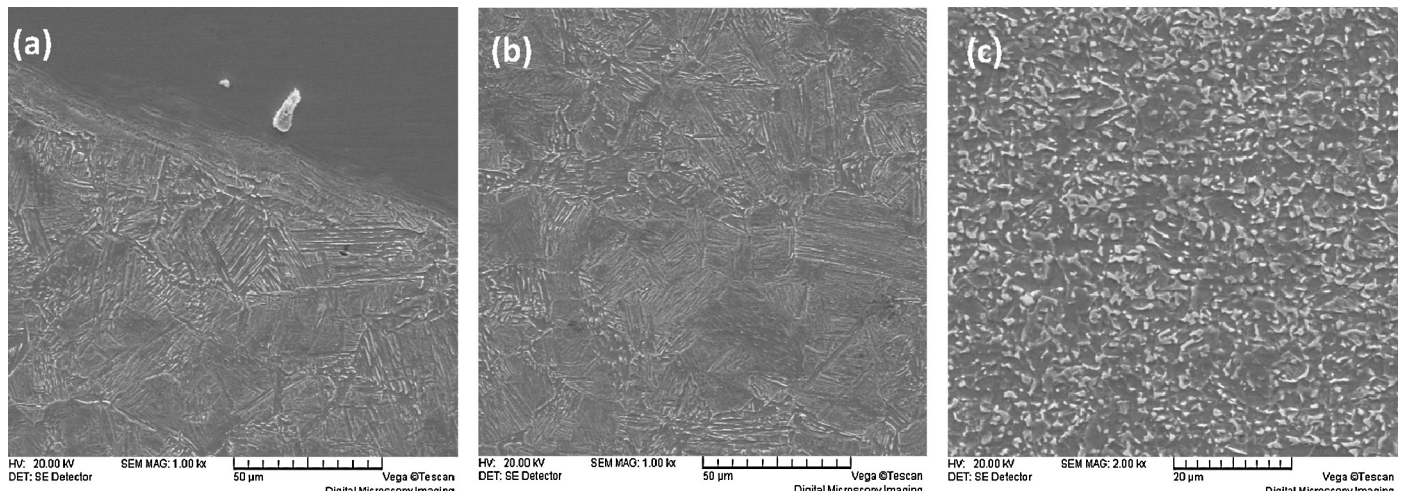


Fig. 15. Microstructure of transverse sections of the 2Cr13Mn9Ni4/Q235B joint at the Q235B side: (a) near the welding interface, (b) WNZ at the Q235B side, and (c) Q235B base metal.

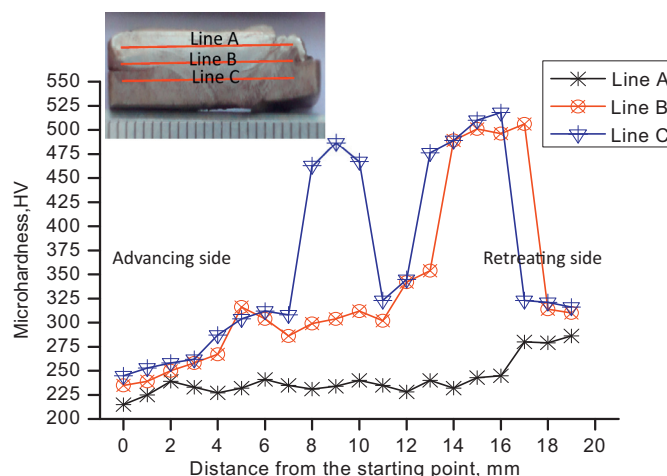


Fig. 16. Microhardness distribution in the 2Cr13Mn9Ni4/Q235B joint.

the Q235B side had relatively higher carbon content and a lower cooling speed, which caused the material to experience a longer time of high temperature. Therefore, large grains of lath martensite were formed at the Q235B side.

4.2.2. Microhardness

Fig. 16 shows the microhardness distribution along the joint cross section. Line A and Line B locate at the 2Cr13Mn9Ni4 and the Q235B sides, respectively. The microhardness along Line A exhibited little variation except for that at the retreating side (at the right side of Line A). Most part of Line B locates in the mechanical interlock zone. A high-hardness area was found along Line B and may locate at the 2Cr13Mn9Ni4 side near the mechanical interlock zone, where the acicular martensite was formed. There were two high-hardness areas along Line C. This can be attributed to the lath martensite obtained at the Q235B side near the mechanical interlock zone.

The microhardness in the mechanical interlock zone is a little higher than that of the 2Cr13Mn9Ni4 and Q235B base metal, and the microstructure in the mechanical interlock zone was composed of austenite and pearlite microstructure. No phase transformation happened in the mechanical interlock zone in the welding process. However, the microhardness of both the 2Cr13Mn9Ni4 and Q235B steel side adjacent to the mechanical interlock zone was

much higher than that of the base metal of the two materials. The high hardness values may be attributed to the martensite formed in these areas. Moreover, the microhardness at the retreating side was higher than that at the advancing side, which is due to the extruded microstructure at the retreating side.

5. Conclusions

- Higher electric current intensity refined the welding's arc-shaped features.
- For AZ31B Mg alloy, the WNZ grains were significantly refined in EFSW joints. The minimum grain size, which was smaller than 1 μm, was observed in the joint under 150 A current. High microhardness values were obtained in the WNZ of AZ31B EFSW joints.
- TMAZ grains in AZ31B EFSW joints were more uniform compared with those in the conventional FSW joint. Twin crystals appeared in the TMAZ of the AZ31B joint under 150 A current.
- In Al 7075 joints, increasing the electric current from 0 to 150 A, led to a grain size increase, from 7 to 11 μm.
- The additional electric current made the strip-shaped grains in the TMAZ of Al 7075 joints less narrow and more equiaxed.
- For both AZ31B and Al 7075 joints, the hybrid heat coarsened the grains in the HAZ, and the minimum microhardness was found at the HAZ under 150 A current.
- EFSW appeared suitable for joining high-strength alloys such as 2Cr13Mn9Ni4 and Q235B. High-microhardness values were obtained at both sides of the mechanical interlock zone.

Acknowledgements

The authors gratefully acknowledge the support of National Natural Science Foundation of China (No.51075413) and the University Excellent Talents Project from Chongqing Municipal Education Commission. The authors would also like to thank Prof. Q. Wang, Dr. Q.Z Liu, Mr. F. Li, H. Wang for helpful discussion.

References

- Afrin, N., Chen, D.L., Cao, X., Jahazi, M., 2008. Microstructure and tensile properties of friction stir welded AZ31B magnesium alloy. *Mater. Sci. Eng. A* 472, 179–186.
- Babu, S.S., Santella, M.L., Feng, Z., Riemer, B.W., Cohron, J.W., 2001. Empirical model of effects of pressure and temperature on electrical contact resistance of metals. *Sci. Technol. Weld. Join.* 6, 126–132.
- Bang, H.S., Bang, H.S., Song, H.J., Joo, S.M., 2013. Joint properties of dissimilar Al6061-T6 aluminum alloy/Ti-6%Al-4%V titanium alloy by gas tungsten arc welding assisted hybrid friction stir welding. *Mater. Des.* 51, 544–551.

- Çam, G., 2011. Friction stir welded structural materials: beyond Al-alloys. *Int. Mater. Rev.* 56, 1–48.
- Chang, K., Feng, W.M., Chen, L.Q., 2009. Effect of second-phase particle morphology on grain growth kinetics. *Acta Mater.* 57, 5229–5236.
- Fazel-Najafabadi, M., Kashani-Bozorg, S.F., Zarei-Hanaki, A., 2011. Dissimilar lap joining of 304 stainless steel to CP-Ti employing friction stir welding. *Mater. Des.* 32, 1824–1832.
- Galler, M., Enzinger, N., Sommitsch, C., 2010. The estimation of the contact interface temperature during resistance spot welding of zinc coated steels using numerical technique. *Mater. Sci. Eng.* 41, 925–930.
- Ilman, M.N., Kusmono Iswanto, P.T., 2013. Fatigue crack growth rate behaviour of friction-stir aluminium alloy AA2024-T3 welds under transient thermal tensioning. *Mater. Des.* 50, 235–243.
- Khodir, S.A., Shibayanagi, T., 2007. Dissimilar friction stir welded joints between 2024-T3 aluminum alloy and AZ31 magnesium alloy. *Mater. Trans.* 48, 2501–2505.
- Luo, J., 2007. Method and Equipment of Resistance-Friction Stir Welding Heat Source. Chinese Invention Patent Application No. 200710092974.7.
- Luo, J., Li, F., Chen, W., 2013. Experimental researches on resistance heat aided friction stir welding of Mg alloy. *Q. J. Jpn. Weld. Soc.* 31, 65s–68s.
- Luo, J., Wang, X.J., Wang, J.X., 2009. New technological methods and designs of stir head in resistance friction stir welding. *Sci. Technol. Weld. Join.* 14, 650–654.
- Park, K., (Ph.D. thesis) 2009. *Development and Analysis of Ultrasonic Assisted Friction Stir Welding Process*. University of Michigan, USA.
- Rogeon, P., Carre, P., Costa, J., Sibilia, G., Saïndrenan, G., 2008. Characterization of electrical contact conditions in spot welding assemblies. *J. Mater. Process. Technol.* 195, 117–124.
- Santos, T.G., Vilac, P., Miranda, R.M., 2011. Electrical conductivity field analysis for evaluation of FSW joints in AA6013 and AA7075 alloys. *J. Mater. Process. Technol.* 211, 174–180.
- Song, K.H., Tsumura, T., Nakata, K., 2009. Development of microstructure and mechanical properties in laser-FSW hybrid welded. *Mater. Trans.* 50, 1832–1837.
- Song, Q., Zhang, W., Bay, N., 2005. An experimental study determines the electrical contact resistance in resistance welding. *Weld. J.* 84, 73s–76s.
- Sun, Y.F., Konishi, Y., Kamai, M., Fujii, H., 2013. Microstructure and mechanical properties of S45C steel prepared by laser-assisted friction stir welding. *Mater. Des.* 47, 842–849.
- Wang, D.Y., Feng, J.C., 2003. Process model of arc corrugation on friction stir weld (in Chinese). *Trans. China Weld. Inst.* 24, 42–44.
- Yang, J., Xiao, B.L., Wang, D., Ma, Z.Y., 2010. Effects of heat input on tensile properties and fracture behavior of friction stir welded Mg-3Al-1Zn alloy. *Mater. Sci. Eng. A* 527, 708–714.